PROSTATE TISSUE DIAGNOSIS USING QUANTITATIVE PHASE IMAGING TECHNIQUES

BY

SHAMIRA SRIDHARAN

THESIS

Submitted in partial fulfillment of the requirements
for the degree of Master of Science in Bioengineering
in the Graduate College of the
University of Illinois at Urbana-Champaign, 2012

Urbana, Illinois

Adviser:

Assistant Professor Gabriel Popescu

Abstract

The lifetime risk of a man getting diagnosed with prostate cancer is 1 in 6. The diagnosis is made by the pathologist using staining methods and immunohistochemical markers to detect malignancy on tissue biopsy sections. Quantitative phase imaging methods eliminate the need for stains and markers. It exploits the intrinsic contrast from the refractive index differences in tissue. The quantitative nature of this technique eliminates inter-observer variability. QPI is sensitive to sub-nanometer level changes in tissue architecture. Light scattering information is also accessible from QPI images since it records both the amplitude and the phase of light that passes through the sample. In this thesis, I show the ability of QPI to distinguish between cancerous and benign samples. I also show its ability to detect changes in stroma and nuclei through different stages of prostate cancer progression that are not detectable using conventional methods.

Contents

1. Introduction

1.1 Overview

Optically thin slices of tissue do not significantly scatter or absorb light. Due to its transparent nature, in clinical pathology, contrast is extrinsically generated by adding dyes to make structures visible. Tissue biopsy sections are traditionally stained with hematoxylin and eosin (H&E). Hematoxylin stains nucleus in a deep blue-purple by a reaction that is not completely understood, whereas eosin non-specifically stains proteins pink and makes the cytoplasm and extra-cellular matrix visible[1]. When the pathologist suspects the presence of cancer on the H&E stained biopsy, a consecutive biopsy section is stained with specialized stains, immunohistochemical markers and/or molecular markers to make a final diagnosis. These techniques can be expensive and time-consuming.

Cells and tissue have intrinsic contrast in the form of refractive index differences between various structures. In the 1930s, Zernike developed phase contrast microscopy in which the unscattered and scattered components of light are separated by a $\pi/2$ phase value, making transparent structures visible[2]. However, phase contrast images are qualitative. Quantitative phase imaging (QPI) techniques image transparent structures and quantitate the change in the path length of light as it transmits through these structures. In constant thickness samples such as tissue sections, the phase value is only dependent on the refractive index. QPI techniques are sensitive to path length changes at the nanoscale level.

In tissue, nanoscale fluctuations in path length correspond to changes in tissue architecture. Light scattering parameters can also be obtained from quantitative phase images. This scattering information and quantitative phase information can be used in the diagnosis of disease. In the

past, QPI has been used to diagnose prostate cancer in label-free tissue biopsies[3]. In this thesis, I describe the utility of QPI in studying optical changes in prostate tissue of varying severity of cancer.

1.2 Outline

In chapter 2, I elaborate on the interaction between light and tissue, and how information about light scattering through various structures can be retrieved from quantitative phase images.

In chapter 3, I present the problems associated with prostate cancer diagnosis, more specifically, benign mimickers of prostate cancer and discuss the importance of prognostic tools.

In chapter 4, I introduce gradient field microscopy (GFM) which is a quantitative tool that can help in separating prostate cancer from its benign mimickers by detection of the basal cell layer (myo-epithelial layer) that is absent in prostate cancer.

In chapter 5, I discuss spatial light interference microscopy (SLIM), a quantitative phase imaging method and Fourier transform light scattering (FTLS), a tool to study tissue scattering. I show some results on the utility of SLIM in detection of changes in stroma of prostate cancer of various Gleason grades and FTLS changes in nuclei of various stages of prostate disease.

Finally, I summarize this thesis and discuss the future direction of this research.

2. Light-tissue interaction[1]

When light is propagated through tissue, there is a change in the irradiance, spectrum, polarization, phase, direction and coherence due to which information about tissue can be obtained [4-6]. The light-tissue interaction can be classified as elastic and inelastic. Elastic light scattering occurs when the frequency of light is conserved. This is different from dynamic light scattering where Doppler shifts caused by dynamic specimen such as live cells cause small changes in light frequency[7]. In diseases such as cancer, the morphological changes in tissue modify light properties such as scattering parameters and this can be used to diagnose disease. Tissue scattering basics are reviewed in this chapter in greater detail.

While inelastic interactions such as emission and absorption are out of the scope of this thesis, spectral changes due to elastic scattering can hinder measurements based on inelastic interactions between light and tissue and is discussed in greater detail below[8].

2.1 Scattering window

Biological tissue and cells is composed of various structures and organelles that have different refractive indices. This difference in refractive index makes tissue highly scattering. The optical microscope is a scattering instrument that makes measurement in real space (x,y,z)[9].

The three major structures in cell are cell membrane, nucleus and cytoplasm. The cell membrane encompasses the cytoplasm and is made of a phospholipid bilayer composed of proteins and glycoproteins that float on lipids. The cytoplasm encompasses cytosol in which various

[1] The text in this chapter is adapted from:
Kim, T., **Sridharan, S.,** Popescu, G. *Fourier transform light scattering of tissues* in Coherent-domain optical methods, Second Edition, Edited by Tuchin, V.V., Springer (2012).
Zhu, R., **Sridharan, S.,** Tangella, K., Balla, A., Popescu, G. *Correlation induced spectral changes in tissues*. Optics Letters 36(21), 2011.

organelles such as mitochondria, golgi apparatus, endoplasmic reticulum, peroxisomes, lysosomes are suspended. The cell nucleus is separated from the cytoplasm by the nuclear envelope and is the site of DNA replication and RNA translation[10].

The different cellular structures have different refractive indices due to varying compositions. This makes the cell a scattering medium. Large structures such as nucleus scatter light at smaller angles whereas smaller organelles such as mitochondria scatter at large angles[11, 12].

Light is absorbed by cells in accordance with the Beer-Lambert's law which helps quantitate the decrease in intensity as light travels through material of thickness L:

$$I = I_0 e^{-\varepsilon \rho L}$$
$$= I_0 e^{-\alpha L}$$

Where ε is the extinction coefficient, ρ is the concentration of absorbing material and α is the absorption coefficient. Since the human body is primarily composed of water, it is important to note that water does not absorb light significantly in the 200-1300nm spectral region as shown by studies by Hale and Querry [13]. Hemoglobin, a red blood cell protein that transports oxygen to tissue, is also a major contributor to the absorption spectrum[14]. Hemoglobin gets oxygenated by binding oxygen to iron atoms as red blood cells pass through the lungs and gets deoxygenated in tissue, changing its absorption spectrum. Hemoglobin absorbs most in blue and green spectral regions.

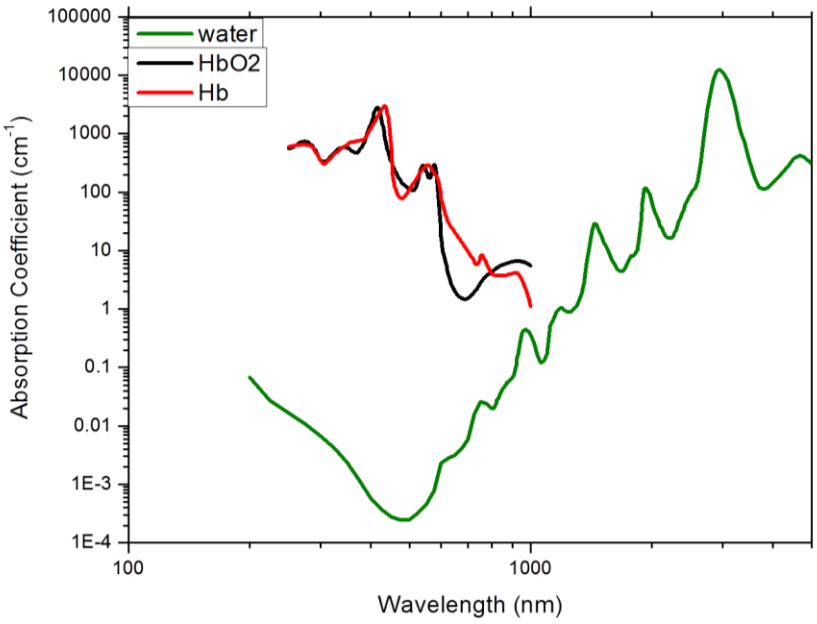

Figure 1[2]: The graph for absorption coefficient vs. wavelength is shown for water, hemoglobin and deoxygenated hemoglobin. From the absorption spectra, the tissue optical window can be obtained.

In the 800-1300nm window, also referred to as the tissue optical window, the tissue exhibits low light absorption. In this window, the scattering effect is dominant and absorption is an insignificant contributor. This is the spectral region where tissue scattering experiments are performed.

2.2 Scattering phase theorem

Scattering phase theorem allows us to calculate the scattering mean free path (l_s) and optical anisotropy (g) from the phase distribution in a tissue section of thickness L<< l_s [15, 16].

[2] Figure adapted from Kim, T., **Sridharan, S.**, Popescu, G. Fourier transform light scattering of tissues in Coherent-domain optical methods, Second Edition, Edited by Tuchin, V.V., Springer (2012).

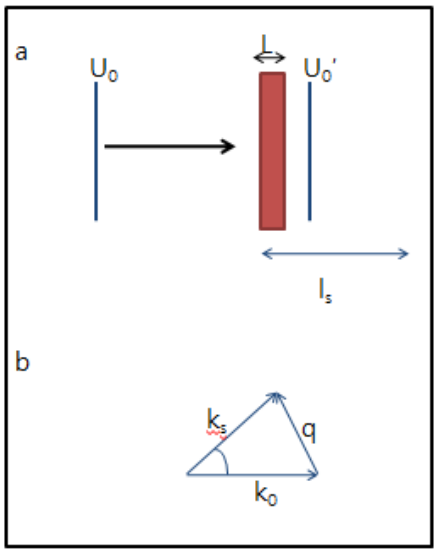

Figure 2[3]: (a): Light with amplitude U_0 travels through tissue section of thickness L for which ls is the scattering mean free path. (b): k_0 is the incident wave vector and k_s is the scattered wave vector, q represents transfer of momentum, g is the optical anisotropy where g=cos θ

The scattering mean free path (l_s) is defined from the Lambert-Beer's law as the length over which the intensity of unscattered light drops to 1/e of its original value. In tissue, this is the average step between two scattering events. l_s is inversely proportional to the phase variance averaged over a certain tissue region as shown in equation[15] (1).

$$l_s = \frac{L}{< \Delta\phi^2(r) >_r} \qquad (1)$$

Optical anisotropy is defined as the average cosine of the angle associated with a single scattering event. It is the change in the direction of light propagation due to scattering. g accounts for forward scattering and scales l_s to a higher value called transport mean free path (l_t

[3] Figure adapted from Kim, T., **Sridharan, S.**, Popescu, G. Fourier transform light scattering of tissues in Coherent-domain optical methods, Second Edition, Edited by Tuchin, V.V., Springer (2012).

) where $l_t = l_s /(1-g)$. Optical anisotropy is related to both the phase gradient distribution and scattering mean free path in the region of interest as shown in equation[15] (2).

$$g = 1 - (\frac{l_s}{L})^2 \frac{\left\langle \left| \nabla[\phi(r)] \right|^2 \right\rangle_r}{2k_0^2} \qquad (2)$$

From the scattering phase theorem, it is evident that when the inhomogeneity in tissue is increased, the propagated light is scattered more which means the optical anisotropy value increases while the scattering mean free path reduces in length.

2. 3 Correlation induced spectral changes in tissue

Correlation induced spectral shifts or Wolf shifts refers to Wolf's prediction that spatial correlations in a primary source affects the optical spectrum in the far zone[17]. These predictions were experimentally confirmed in acoustic waves, spectroscopic measurements on stellar objects and scattering media[18-21]. The frequency shift in spectral lines was explained by the medium scattering various wavelengths with differing strength which was dependent on the scattering angle[20].

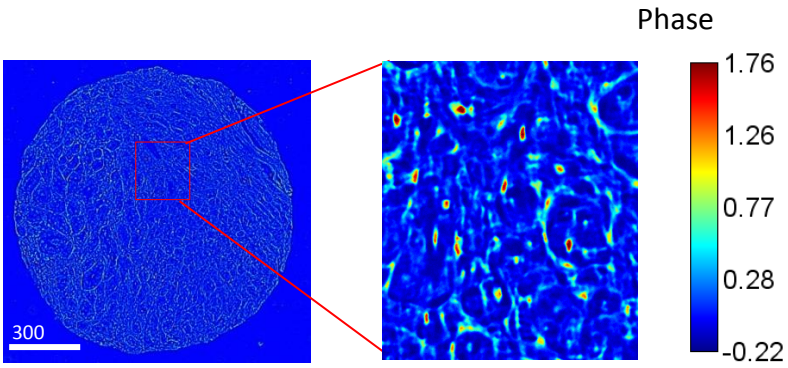

Figure 3[4]: A quantitative phase image of a prostate tissue microarray core of 4micron thickness with a region zoomed in.

[4] Figure reprinted from Zhu, R., **Sridharan, S.**, Tangella, K., Balla, A., Popescu, G. *Correlation induced spectral changes in tissues*. Optics Letters 36(21), 2011.

We measured this spatial correlation function on a quantitative phase image of an unstained 4μm thick prostate cancer tissue section which is shown in Fig. 3.

We calculate the optical spectrum associated with scattering angle θ by starting with the Helmholtz equation:

$$\Delta^2 U(r,\omega) + k_0^2 U(r,\omega) = -k_0^2 \chi(r) U(r,\omega)$$

Where k0 is the incident wave vector, χ is the dielectric susceptibility of optically thin specimen and the field is a function of the angular frequency ω and spatial coordinate r. According to the Born approximation, the incident plane wave remains a plane wave inside the tissue. By applying the Born approximation to (3) we get:

$$\nabla^2 U(r,\omega) + k_0^2 U(r,\omega) = -k_0^2 \chi(x,y)\delta(z) A(\omega) e^{ik_0 z}$$

Where $A(\omega)e^{ik_0 z}$ is the incident plane wave. We take the Fourier transform of the above equation with respect to r to obtain the field in wave vector form

$$\tilde{U}(k,\omega) = \frac{k_0^2}{k^2 - k_0^2} A(\omega) \tilde{\chi}(|k| - k_i)$$

The above equation expression is a variation of diffraction tomography in which the scattered field measured along the wave vector direction provides information about the spatial frequency component $q=k-k_i$. The scattering angle θ is related to the momentum transfer q by $q=2k_0\sin(\theta/2)$. The susceptibility term is only dependent on k_x and k_y, so we define a new term $k_\perp = (k_x^2 + k_y^2)^{\frac{1}{2}}$ and therefore $Q^2 = (k_0^2 - k_\perp^2)$ and equation 3 becomes:

$$\tilde{U}(k,\omega) = \frac{k_0^2}{2Q}\left(\frac{1}{Q-k_z}+\frac{1}{Q+k_z}\right)A(\omega)\tilde{\chi}(k_\perp)$$

We obtain the scattered field in spherical terms by taking the 1D inverse Fourier transform with respect to k_z

$$\tilde{U}(k_\perp,z,\omega) = \frac{k_0^2}{2}A(\omega)\tilde{\chi}(k_\perp)\left(\frac{e^{iQz}}{Q}+\frac{e^{-iQz}}{Q}\right)$$

We ignore the term e^{-iQz}/Q since it corresponds to the angular backscattering term. We express this in terms of the power spectrum, which is the square of the amplitude term:

$$S(\theta,\omega) = \left(\frac{k_0}{2\cos\theta}\right)^2 \tilde{\chi}^2(k_\perp)S_i(\omega)\Big|_{k_0=\omega/c}$$

Where $\cos\theta = Q/k_0$, $k_\perp = k_0\sin\theta$ and S_i is the incident power spectrum. This expression shows that the optical spectrum at distinct scattering angles is dependent on both the incident spectrum and the spatial power spectrum of the scattering tissue which is expressed as $\tilde{\chi}^2(k_\perp)$. The distinct spatial frequencies of the medium can be viewed as a sinusoidal grating which diffracts longer wavelengths at larger angles. The Wolf effect is the average result of this diffraction effect.

We calculated the refractive index distribution n(x,y), the susceptibility $\chi(x,y)$ and power spectrum $\left|\tilde{\chi}(k_x,k_y)\right|^2$ from the quantitative phase image of the 4μm thick tissue section shown in fig 1. The sample was imaged with white light of a Gaussian spectrum centered at 4×10^{15} rad/s and a standard deviation 1×10^{14} rad/s. We used equation 7 to calculate the spectrum of scattered light.

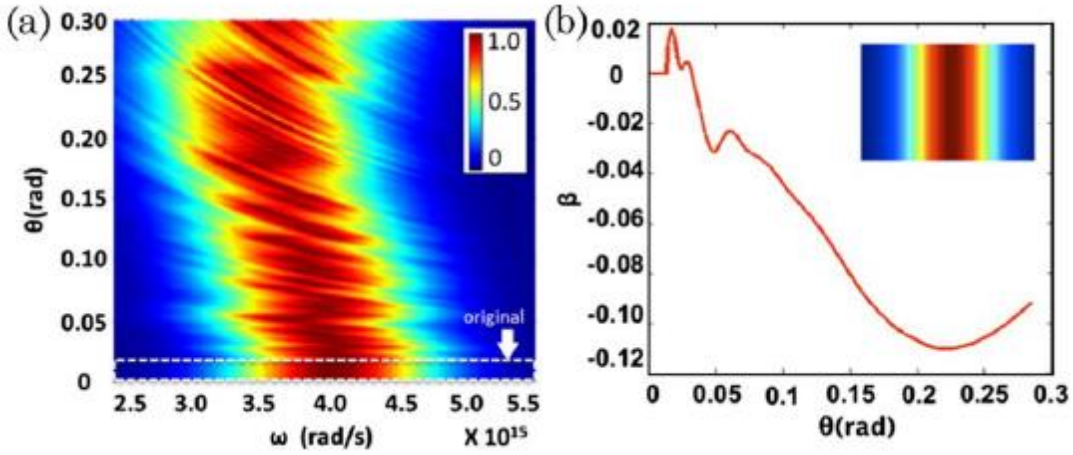

Figure 4[5]: (a): Spectrum Vs Angle for scattered light from the tissue in Fig 1 (b): The relative change of mean frequency; negative values correspond to a shift in the red light spectrum.

When we closely examine the scattered spectrum at each angle, we notice that there is a modification from the original spectrum with red spectral shifting (Fig 3a). This is consistent with static scattering. We quantified the overall shift by defining $\beta(\theta) = (\omega_0' - \omega_0)/\omega_0$ where ω' is the shift in mean frequency and ω_0 is the original mean frequency. The red shifts are significant (Fig 3b). The maximum shift in red is more than 10%. By plotting the spectrum in absence of correlations, we see that the normalized spectrum at different angles does not change (Fig 3b inset). This proves that the shift is entirely due to spatial correlations.

Our study shows that the measured scattering spectrum at various angles is affected by tissue spatial correlations. These spatial correlations change the shape of the emitted field without affecting the emission process. This effect can cause errors in spectroscopic measurements of tissue due to the significant effect in angular and spectral resolved measurements. This can be resolved by simultaneous measurement of morphology and spectroscopy.

[5] Figure reprinted from Zhu, R., **Sridharan, S.**, Tangella, K., Balla, A., Popescu, G. *Correlation induced spectral changes in tissues*. Optics Letters 36(21), 2011.

3. Prostate Cancer

The prostate is an exocrine gland weighing 30-40g in the adult male reproductive system that is located at the base of the urinary bladder. The urethra and the ejaculatory duct pass through the prostate gland. The prostate secretes 12% of the ejaculatory fluid into the duct which opens into the prostatic urethra [22]. In 1968, McNeal performed serial sectioning of the prostate gland to study the various structures within the prostate. The gland can be divided into four zones. The central zone comprises approximately 25% of the gland and surrounds the ejaculatory duct. It consists of large acini with irregular contours that project into the lumen of the gland; the epithelium comprises big nuclei in a crowded arrangement with granular cytoplasm [23, 24]. The peripheral zone, which comprises 70% of the prostate, surrounds the distal region of the urethra and has small acini with smooth walls; the epithelium has pale cytoplasm with small basal nuclei [24]. Most cases of prostate cancer arise within the peripheral zone of the prostate gland [25]. The third zone is the transition zone which comprises 5% of the prostate and surrounds the proximal portion of the urethra; the epithelium is histologically similar to the peripheral zone [24]. Most cases of benign prostatic hyperplasia arise in the peripheral zone of the prostate gland [26]. The fourth zone of the prostate is the anterior fibromuscular stroma, which is a non-glandular region anterior to the prostate gland [23].

The acini of the prostate open into prostatic ducts which in turn secrete into the prostatic urethra. The acinar cells primarily are made of columnar epithelium, neuroendocrine cells and basal cells [22, 27]. The columnar epithelial cells are 10-12μm in size and secrete prostate specific antigen (PSA) and prostatic acid phosphatase (PAP); it also requires androgen for maintenance [23]. Neuroendocrine cells are scattered throughout the acini and basal cells rest on the basement

membrane [23]. Prostatic stroma is a collection of various cell types, such as fibroblasts, smooth muscle cells, blood, lymphatic vessels and autonomic nerve fibers [28].

The most common initial symptom of prostate disorder is urinary difficulty, since the urethra passes through the prostate gland. A person might get a needle biopsy to check for prostate cancer if their serum PSA reading is above the normal cut-off of 4.0ng/L or suspicion during a digital rectal exam (DRE). The needle biopsy specimen is embedded in paraffin and sliced using a microtome. The tissue slice is then placed on a glass slide and stained with hematoxylin and eosin (H&E) stain. The pathologist examines the H&E stained biopsy for the presence of the basal or myo-epithelial layer to exclude the diagnosis of prostate cancer. The basal cell membrane is breached in prostate cancer and cancerous epithelium invades the surrounding stromal region. Conditions such as high-grade prostatic intra-epithelial neoplasia, which is a benign mimicker of prostate cancer, can make the diagnosis difficult. In the following section, I discuss benign prostate conditions and prostate cancer in more detail.

3.1 Benign Prostate Conditions

The two benign prostate conditions that were studied using QPI are benign prostatic hyperplasia (BPH) which commonly affects older men and is often characterized by an enlarged prostate and high grade prostatic intra-epithelial neoplasia (HGPIN) which is a benign mimicker of prostate cancer.

3.1.1 Benign Prostatic Hyperplasia (BPH)

Approximately 50% of all men over the age of 40 will develop benign prostatic hyperplasia (BPH) [29]. BPH is a condition in which the number of epithelial and stromal cells in the prostate is increased. The increased cell count could be due to increased epithelial or stromal

proliferation or decreased rate of apoptosis [30]. BPH is diagnosed on a trans-urethral resection of the prostate (TURP) samples. A diagnosis of BPH cannot be made on a needle biopsy sample since the transition zone is not sampled in most needle biopsies. In our study of prostate conditions, we used tissue from individuals with BPH as control since it's a common condition afflicting individuals in the age-group primarily affected by prostate cancer.

3.1.2 High-grade prostatic intra-epithelial neoplasia (HGPIN)

High-grade prostatic intraepithelial neoplasia (HGPIN) is a benign condition that is considered to be a precursor to prostate cancer [25, 31, 32]. HGPIN is observed in 0 to 24.6% of prostate needle biopsies with mean reported incidence of 7.6% [33, 34]. Prominent nucleoli and presence of Roman bridges are common hallmarks of high-grade PIN [33, 34]. HGPIN is not very common in the transition zone, has evenly spaced glands with focal to no necrosis and patchy basal cell layer distinguishing it from prostate adenocarcinoma [33, 34]. Detection of myoepithelial cells or basal cells by usage of antibody against cytokeratin 34BE12 and/or p63 marker is performed by the pathologist to exclude the diagnosis of carcinoma in suspected cases of HGPIN [34]. The diagnosis of HGPIN is often made in patients suspected of having prostate cancer and usage of special stains can delay diagnosis causing anxiety to patients. In our lab, we developed a qualitative imaging technique, Gradient Field Microscopy (GFM) that detects the basal cell layer in real-time preventing the delays caused by immunostains. GFM is described in detail in the next chapter.

3.2 Prostate Cancer

Cancer statistics from 2010 indicate that prostate cancer is the most commonly diagnosed cancer among men (not including skin cancer) in the United States of America and the second leading cause of cancer-related deaths[35]. The SEER program by National Cancer Institute estimates

that there will be 241,740 new cases of prostate cancer and 28,170 men will die of prostate cancer in the United States in 2012[36]. Due to the high fatality rate and economic costs related to prostate cancer care, there was a need for an early detection tool for prostate cancer.

A good screening tool will diagnose a condition in its early stages and the number of people diagnosed with the condition through screening will stabilize to the pre-screening numbers after an initial spike. The prostate specific antigen test (PSA) was developed to detect early prostate cancer and needle biopsies were performed in individuals with serum PSA above 4.0 ng/L. PSA screening increased the number of people diagnosed with prostate cancer and the numbers did not go down to the pre-screening era levels [37].

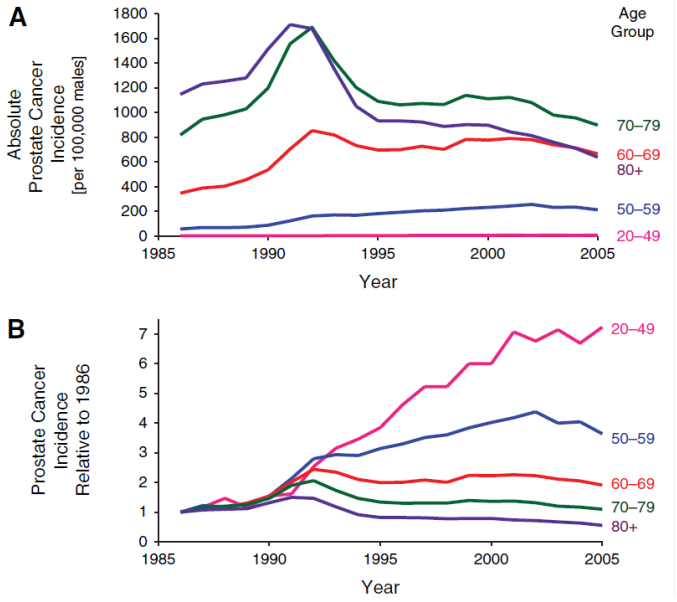

Figure 5[6]: PSA screening was introduced in 1986. Panel A shows that while the spike associated with screening reduced, it did not stabilize to pre-screening levels. Panel B shows the increasing trend in the ratio of prostate cancer incidence relative to 1986 when screening was first introduced.

[6] Figure reprinted from Welch, H.G. and P.C. Albertsen, *Prostate cancer diagnosis and treatment after the introduction of prostate-specific antigen screening: 1986-2005.* Journal of the National Cancer Institute, 2009. **101**(19): p. 1325-9.

The median age of diagnosis of prostate cancer is 67 years while the median age of death due to prostate cancer is 80 years with 71% of death due to disease occurring at age above 75 years [36]. Hence, in 2008, the United States Preventive Services Task Force recommended against PSA screening for men over the age of 75 years [38]. Further studies showed that while the life-time risk for prostate cancer diagnosis is 15.9%, the risk of dying of the disease is 2.8% and that 1.2 million new cases of prostate cancer would be diagnosed if all American men between the ages of 62 and 75 years underwent prostate biopsy [39]. Studies have shown that 1/3rd of all men in the age group of 40-60 years and 3/4th of all men above the age of 75 years have histologic prostate cancer [40, 41]. Out of every 1000 men who undergo surgery to treat prostate cancer, 10-70 men suffer serious complications; 200-300 men have undesirable long-term effects such as bowel dysfunction, urinary incontinence and erectile dysfunction[42]. Based on these findings, the USPSTF recommended against PSA screening for men of all ages in 2012 [39].

Current data and research indicate that prostate cancer is over-diagnosed. Among men affected by the disease, some have asymptomatic slow growing tumors while others have a more aggressive form of the disease which requires early and aggressive intervention. Hence there is a need for prognostic tools in prostate cancer such as Gleason grading.

3.2.1 Gleason Grading of Prostate Cancer

The Gleason grade is the most widely used grading scheme in prostate cancer. The system was developed by Dr. Donald Gleason in the 1960s and is based on glandular differentiation seen in hematoxylin and eosin (H&E) stained slides [43, 44]. The Gleason score has been proven to be an indicator of tumor size, metastasis, treatment and outcome [44-47].

The variation in grades on a scale from 1-5, in order of increasing severity, is based on glandular differentiation and glandular presence in stroma [43, 44, 48, 49]. The primary grade is the pattern present in maximum biopsy area and the secondary grade is the second most prominent pattern. The secondary area has to encompass atleast 3% of total biopsy area [50]. The two grades are added to provide a Gleason score of 1-10. More recently, tertiary patterns are reported (area <5%) on the pathology report if it is of Grade 4 or 5 due to possible presence of metastasis [51].

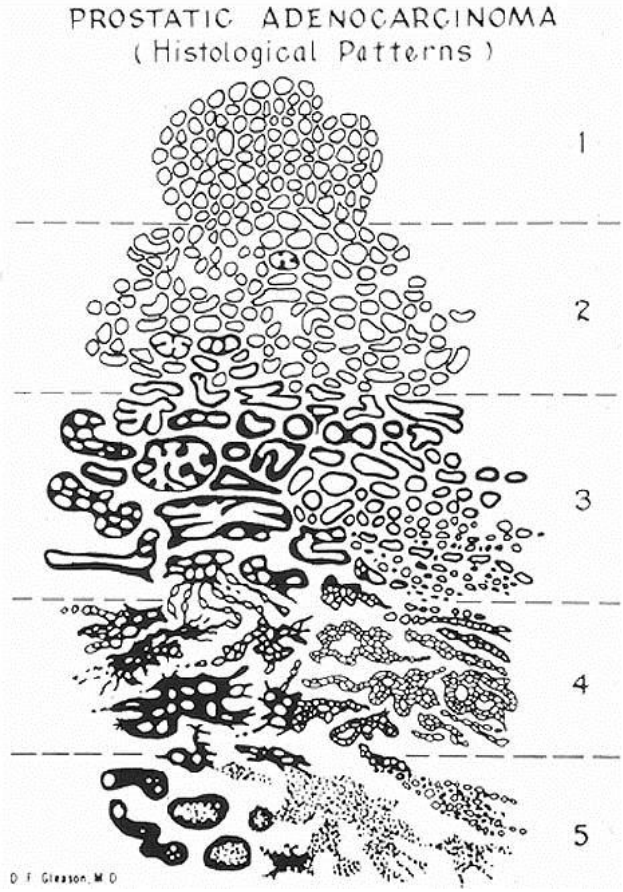

Figure 6[7]: Standard drawing of Gleason grading system made by Dr. Donald F. Gleason

[7] Figure reprinted from Gleason, D.F., *Classification of prostatic carcinomas.* Cancer Chemother Rep, 1966. **50**(3): p. 125-8

A modified Gleason grading system was adopted in 2005 at the United States and Canadian Academy of Pathology meeting [52]. Gleason grading is done at 4X or 10X magnification with confirmation at 20X or 40X to detect fusion of glands and necrosis.

In current clinical practice, cancer of Gleason grade 1 is rarely diagnosed. It is suspected that immunostains would re-label the cases categorized by Dr. Gleason as Grade 1 would be re-categorized as adenosis and some cases of cribriform grade 3 adenocarcinoma as high-grade prostatic intra-epithelial neoplasia (HGPIN) [33, 53].

Gleason grade 2 consists of irregular glands that are smaller than normal, but larger than other cancerous glands and the tumor is well circumscribed. The cribriform pattern described by Dr. Donald Gleason is no longer considered Gleason grade 2 [33, 52]. Gleason grade 2 is rarely diagnosed due to poor reproducibility among pathologists and poor correlation on radical prostatectomy specimen [33]. The diagnosis of Gleason score 2-4 (grades 1,2) has decreased from 24% in 1991 to 2.4% in 2001 [54].

Gleason grade 3 glands are medium to small size, singular with infiltrating edges [44]. The cribriform (gland within gland pattern) is also observed in Gleason grade 3, however, they do not have necrosis [44]. Cribriform Gleason grade 3 glands resemble HGPIN glands with the absence of basal cell layer, reduced spacing between glands and possible perineural invasion or extra-prostatic extension [33]. Singular cells as described by Dr. Gleason are no longer considered grade 3 [52].

Gleason grade 4 consists of small glands that are fusing into one another and cribriform patterns with irregular edges as opposed to the smooth edges seen in cribriform glands of Gleason grade 3

[33]. Gleason grade 4 also has a hypernephromatoid subtype which has similar glandular pattern as other grade 4 glands but has cleared cytoplasm resembling renal cells [43].

Gleason grade 5 comprises of sheets or cords of cells with no glandular differentiation [43]. A cribriform pattern that looks like Gleason grade 4 with central region displaying necrosis, termed comedonecrosis is also considered Gleason grade 5 pattern [44].

Gleason scores are often grouped together as score 2-4: well-differentiated; score 5-6: moderately differentiated; score 7: moderately to poorly differentiated and 8-10: poorly differentiated [33]. There have been studies that have shown that Gleason score 7 is a heterogeneous disease with differential outcomes for Gleason grade 4+3 as opposed to Gleason grade 3+4 [33, 55]. However, there are also studies disputing this finding [56-58]. The reasons for this disagreement in results could be the inter-observer differences reported in Gleason grading or the difference between the grades seen in needle biopsy and prostatectomy specimen [59-61].

In this thesis, I studied differences in the stroma adjoining the gland of Gleason grade 3 and Gleason grade 4 glands to explore the possibility of Gleason score 7 being a heterogeneous disease. I also studied the difference in nuclear scattering in prostate tissue of varying levels of glandular differentiation. This is explained in detail in Chapter 5.

4. Qualitative Diagnosis Methods[8]

The distinction between cancer and normal biopsies is made by the detection of basal cell layer. Gradient field microscopy (GFM) is a high contrast method that detects these basal cells. GFM also has the advantage of high acquisition speed. Since the contrast is increased optically, there is no need of post-image processing. Thus, GFM naturally provides an ability to image in real-time and the acquisition speed is limited only by the acquisition speed of the detector used in the setup.

4.1 Gradient Field Microscopy (GFM)

Figure 1 shows the setup for gradient field microscopy (GFM), which is an experimental setup for the Fourier filtering using a sinusoidal amplitude mask. GFM is built as an additional module to a commercial bright field microscope, which is composed of the components from the condenser lens to the tube lens. The aperture stop closed down to the minimum size in order to obtain high spatial coherence in the white light illumination. From the image plane of the microscope, there is a relay of optical components comprising two lenses to form a 4*f* system and a spatial light modulator (SLM). The first Fourier lens, L1, with the focal distance f_1=75mm is at f_1 away from the image plane, and the SLM is located at f_1 away from L1 which is the Fourier plane of the image plane of the microscope. The second Fourier lens is at its focal distance, f_2=150mm, away from the SLM and forms the modulated image at f_2 away from itself, where the

[8] The text in this chapter is reprinted with permission from:
Kim, T., **Sridharan, S.,** Popescu, G. *Gradient field microscopy of unstained specimens*, Optics Express 20(6), 2012.
Kim, T., **Sridharan, S.,** Popescu, G., *Gradient field microscopy allows label-free disease diagnosis* (invited), Laser Focus World, 48 (8), (2012)
Kim, T., **Sridharan, S.,** Kajdacsy-Balla, A., Tangella, K., Popescu,G.,, *Gradient field microscopy for label-free diagnosis of human biopsies*, Appl. Opt. (Special Issue on Holography), 52 (1), A92-A96 (2013)

detector (Andor iXon^{+} EMCCD) is located. As a whole, GFM module increases the contrast by imaging the first-order derivative of the phase of the sample as well as the magnification determined by the ratio between the two Fourier lenses, which is 2 in our setup.

The SLM in our setup is a liquid crystal panel taken from Epson Powerlite S5 commercial projector sandwiched between two cross polarizers. The top inset of figure 1 is projected to the amplitude SLM and the bottom is the profile of the sinusoidal modulation taken along the dashed line. The contrast ratio of this device, 400/1, provides enough attenuation at where the projected value on the liquid crystal is zero. Furthermore, the sine modulation period is calculated to be 7.8mm (13μm/pixel, 600pixels/period) and it yields the shift of $2\lambda f/a$=20μm between the two separated beams and the DC field locates at the middle of the two beams.

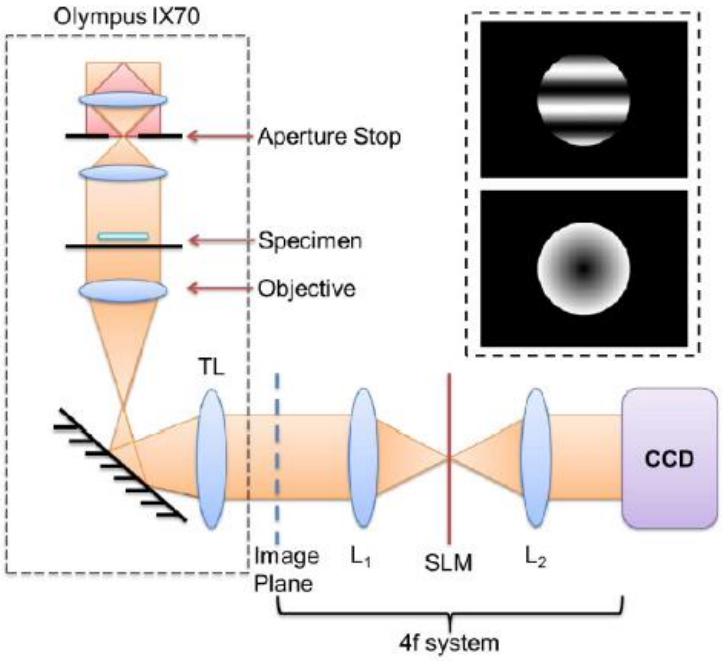

Figure 7[9]: GFM Set-up. The inset shows the modulation filter projected on SLM for sine-GFM (top) and linear-GFM (bottom).

[9] Figure reprinted from Kim, T., **Sridharan, S.,** Popescu, G. *Gradient field microscopy of unstained specimens*, Optics Express 20(6), 2012

4.2 HGPIN Diagnosis using GFM

As mentioned earlier, HGPIN is a benign condition in which biopsy samples have morphological features associated with prostate cancer. The only distinguishing characteristic is the presence of the myoepithelial cell layer in HGPIN biopsies, but not in the cancer biopsies. The myoepithelial cell layer is patchy and is detected with immunohistochemical markers which can delay diagnosis by a day or longer. Due to their small size, there is a sharp change in optical path length at the stroma-epithelium boundary making them clearly visible in GFM images.

We imaged HGPIN samples using the 100X/1.4NA oil immersion objective on the GFM setup. We had to use the mosaic feature and stitched 154 images to obtain the final GFM image. By qualitative examination of the boundary of the stroma and epithelium, we were able to detect the basal cells in the GFM images of cores with HGPIN. These results are shown in the figure below.

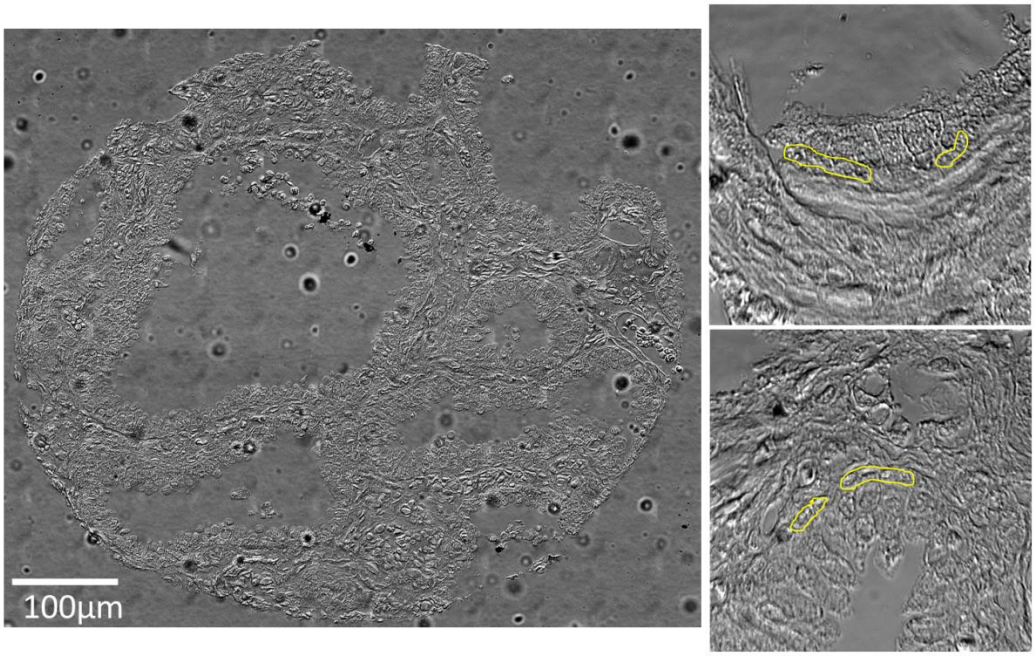

Figure 8[10]: Left shows a prostate tissue microarray core with HGPIN imaged with GFM. Due to its high contrast, edges are prominent. The figures on the right show areas from prostate TMA zoomed in with the basal cell layer highlighted.

[10] Figure reprinted from Kim, T., **Sridharan, S.,** Popescu, G. *Gradient field microscopy of unstained specimens*, Optics Express 20(6), 2012.

5. Quantitative Diagnosis

Zernike developed the Nobel-prize winning technique, phase contrast microscopy, in the 1930s. In a phase contrast microscope, the sample is illuminated by spatially coherent white light. The component of light that passes through cellular structures is retarded in phase, and by adding an additional $\pi/2$ delay to this scattered component, the path-length difference between the scattered and unscattered components of light increases to $\lambda/2$ making transparent objects visible[62]. In the 1940s, Gabor developed holography which enabled the recording of both the amplitude and phase information[63].

Spatial light interference microscopy (SLIM) was developed in the Quantitative Light Imaging (QLI) group at University of Illinois by combining principles from Zernike's phase contrast microscopy and Gabor's holography as a quantitative phase imaging method that is sensitive to path-length changes of upto 0.3nm spatially and 0.03nm temporally[64].

5.1 Spatial Light Interference Microscopy (SLIM)

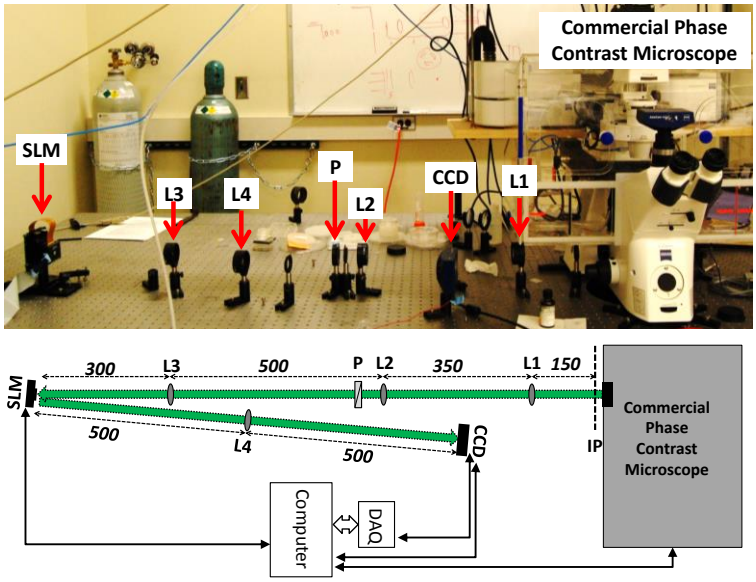

Figure 9: SLIM is an add-on module to a commercial phase contrast microscope.

Spatial light interference microscopy (SLIM) is a quantitative phase imaging method that is described in detail in [64]. Briefly, SLIM is an add-on module to the commercial phase contrast microscope (Zeiss Axio Observer Z1) and adds 3 additional phase shifts in increments of $\pi/2$ to the un-scattered component of light passing through the sample. The SLIM module projects the back focal plane of the objective to the liquid crystal phase modulator which introduces the additional phase shifts. We record 4 intensity images and calculate a quantitative phase map from these images. The final image is calculated by the formula:

$$\phi(x,y) = \frac{2\Pi}{\lambda} \int_0^{h(x,y)} \left[n(x,y,z) - n_0 \right] dz \qquad (54)$$

Each term in this equation is defined as follows.

λ: Central wavelength of light. In SLIM, light used is white light, so it corresponds to 552.3nm, $h(x,y)$: Local thickness fluctuations $n(x,y,z)$: Local refractive index fluctuations, n_0: Refractive index of surrounding medium.

SLIM measures optical path length changes with a sensitivity of 0.3nm spatially which corresponds to dry mass sensitivity of 1.5fg/μm^2[65]. In the past, our group demonstrated that refractive index could be used as a marker to differentiate cancer and normal areas of the prostate as well as to measure cell growth and dynamics[65-68].

5.2 Fourier Transform Light Scattering (FTLS)

QPI techniques such as SLIM record both the amplitude and the phase of the field at the image plane. Since complete information about the field is available, the field distribution at all other planes can be calculated. The image and scattering field have a Fourier transform relationship.

Fourier transform light scattering (FTLS) is a sensitive method to study angular scattering information since the field is measured at the highly uniform image plane [69, 70].

We used SLIM and FTLS to quantitatively study changes in prostate nuclei and stroma through various pathological stages.

5.3 Optical changes in prostate stroma

5.3.1 Motivation

The Gleason grading system focuses primarily on changes in the glandular structure and therefore the epithelium. The immunostains used in prostate pathology, such as high molecular weight cytokeratin, p63 and AMACR focus on various aspects of the epithelium. More recently, some molecular studies have focused on the stroma in prostate cancer.

The stroma is a complex environment consisting of the extracellular matrix, fibroblasts, smooth muscle cells, growth factors, regulatory receptors, blood vessels, nerve fibers and immune cells [28]. In the prostate, the primary stromal components are fibroblasts and smooth muscle cells [71]. The various components of the stroma provide adhesion, growth factor secretion and regulation, structural framework and support, cell attachment and migration and permeability [72, 73]. In response to carcinoma in the epithelium, the repair mechanism in stroma is activated [74]. The stromal changes seen in cancer using immunohistochemistry or molecular studies mimic the changes seen in wound healing mechanisms such as increased growth factor secretion, angiogenesis, matrix remodeling, elevated immune response and increased protease activity [75-79]. These changes also include a switch to the activated myofibroblast phenotype from fibroblast characterized by increased secretion of vimentin and smooth muscle to myofibroblast with reduced levels of α-smooth muscle actin and calponin [74, 77, 78, 80, 81].

We used refractive index as an intrinsic marker to study changes that occur in stroma due to prostate adenocarcinoma of various Gleason grades. In SLIM images, individual strands of stroma are clearly visible. We focused on the layer of stroma immediately adjoining the gland since we hypothesized that the progression of disease should first affect this layer as adenocarcinoma involves epithelial proliferation into the stroma. Our results showed that the variation in the stromal architecture increases with increasing Gleason grade. Since SLIM is sensitive to nanoscale fluctuations in tissue morphology, we believe that the variation we see is indicative of protein expression and distribution changes in various stages of prostate disease.

5.3.2 Materials and Methods

We obtained tissue microarray slides from the TMA2 set of the Co-operative Prostate Cancer Tissue Resource (CPCTR) database at the University of Illinois at Chicago- College of Medicine. TMA2 is a set of 4 slides that contain approximately 1200 cores of Gleason scores 4-10 that are well characterized and graded by consensus among multiple pathologists.

We imaged unstained slides with tissue thickness of 4µm using SLIM. The slides were imaged using the 10X/0.3NA objective and the mosaic feature on the Zeiss microscope for each block comprising of 20 cores. The mosaic feature can be adjusted to set up multiple focus planes, ensuring that all sample areas are in focus. Imaging time for 20 cores with the inclusion of manual work such as setting up the mosaic and focus points is 40 minutes. The images were stitched together using an ImageJ plugin built in-house and individual cores were cropped out to the size of 3000x3000pixels which is approximately 9 frames stitched together.

After the completion of label-free imaging using SLIM, the same slides were sent to Provena Hospital for H&E staining. These slides were then digitized using the Nanozoomer at the

Institute of Genomic Biology, University of Illinois at Urbana-Champaign. Using the information from the CPCTR database, we identified cores with Gleason grade 3 cancer from a final score of 6 and Gleason grade 4 cancer from a final score of 8 (4+4), 7 (4+3) and 9 (4+5). Occasionally, the final Gleason grade diagnosed on the patient and the Gleason grade observed on the tissue sample we obtained are not the same. To eliminate errors due to sampling, our collaborating pathologists confirmed the presence of grade 3 and grade 4 glands in the cores we used for our analysis.

We then segmented individual strands of stroma on the SLIM images on the pathologist-identified glands of a specific grade using ImageJ and a Wacom tablet with the H&E image as a reference for both grade 3 and grade 4. One advantage we had with the SLIM images over H&E stained images is the clear visibility of individual stromal strands between glands, including fusing glands. We calculated the magnitude and standard deviation of the phase and the magnitude of the gradient of the phase in these stromal regions of interest (ROI) using another plugin built in-house combined with the measurement features on ImageJ. With these measurements we were able to calculate the ratio of the phase gradient to the square of the variance, which is related to g (anisotropy factor), the average cosine of the scattering angle associated with a single scattering event [15, 16].

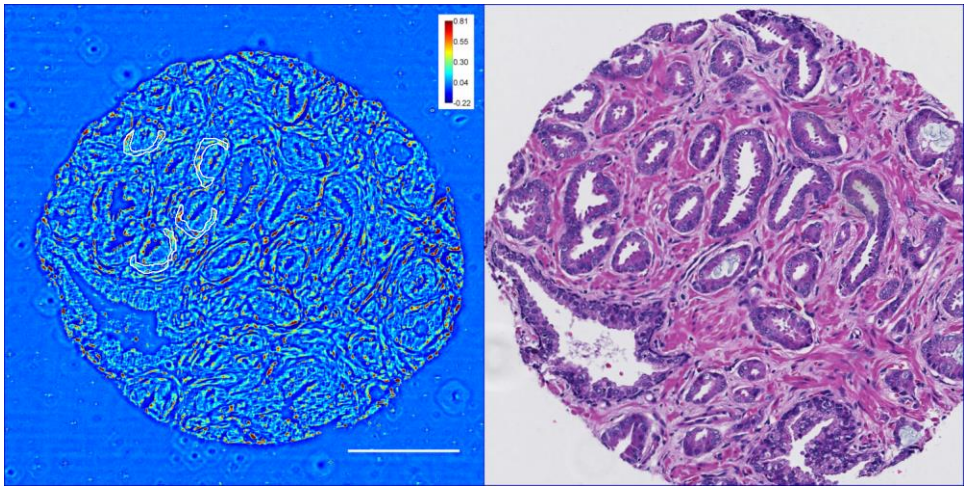

Figure 10: SLIM image with the corresponding H&E image of a tissue microarray (TMA) core of prostate with Gleason score 6 (3+3) adenocarcinoma. On the H&E, pink areas are stroma and the purple areas are nuclei, epithelium. On SLIM, we can clearly see individual strands of stroma even at 10X/0.3NA. The SLIM image is 3000x3000pixels and is approximately 10 images stitched together from the mosaic imaging set up on Zeiss. Also, an individual strand of stroma surround the gland has been marked for 4 glands on the SLIM image.

5.3.3 Results

55 cores with Gleason grade 3 cancer and 55 cores with grade 4 cancer were used for analysis. A single layer of stroma adjoining the gland was segmented to generate 118 ROIs for grade 3 and 117 ROIs for grade 4. We found significant differences in the square of the ratio of phase gradient to phase variance (anisotropy factor analog) as shown in Fig. 4, 5. Using the non-parametric Mann-Whitney test, the values for anisotropy-analog were determined to be higher for grade 4 ($p=3.76E-6$). Also, the value for the magnitude of the phase gradient was higher in cases with grade 4 cancer than grade 3 ($p=7.5E-5$) (results not shown).

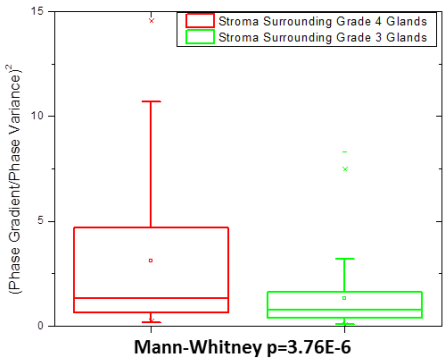

Figure 11: The distribution of anisotropy values is over a wider range for the stroma surrounding grade 4 glands and the difference between the two groups is significant.

We further analyzed Gleason grade 4 stroma since the value of the anisotropy parameter was distributed over a wide range of values. We compared anisotropy values in the grade 4 stroma among 15 patients (34 ROIs) with final diagnosis of Gleason score 8 (4+4) and 16 patients (42 ROIs) with final diagnosis Gleason score 9 (4+5) as shown in Fig. 6. Our analysis showed that the level of disorganization is higher in patients with Gleason score 9 (Mann-Whitney, p=5.91E-5).

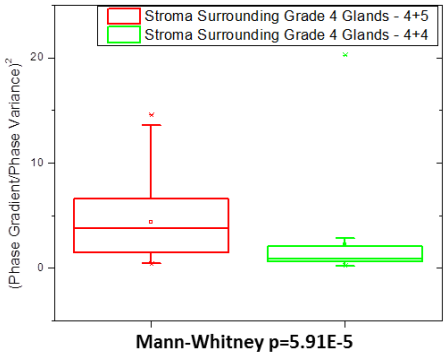

Figure 12: The distribution of anisotropy values is over a wider range for the stroma surrounding grade 4 glands from patients with a final diagnosis of Gleason score 9 (4+5) adenocarcinoma than that of Gleason score 8 (4+4) adenocarcinoma. The difference between the two groups is significant.

5.3.4 Discussion

We calculated the square of the ratio of the phase gradient to phase variance, which is the variable term in the calculation of the anisotropy factor (g). This substitution was made since an anisotropy calculation over a small area of stroma which the number of scattering angles measured. This in turn, pushes g to higher cosine values. Anisotropy is directly related to the optical roughness of the tissue. We can see that the anisotropy is higher for the stroma adjoining glands of grade 4 cancer and the distribution is over a very wide range, whereas for grade 3, the value is small and distributed over a narrow range. These results also translate over when we compare grade 4 regions among patients with final diagnosis of Gleason score 8 and 9. In immunohistochemistry studies performed by other groups, hyaluronan (HA) level was observed to be high in the stroma of prostate biopsies of higher Gleason grades but HA receptor CD 44 level is inversely related to Gleason grade [82]. High platelet-dervived growth factor (PDGFR-β) expression and low expression of whey acidic protein family member WFDC1/PS20 has also been seen in stroma adjoining high Gleason grade glands [83, 84]. In another study, an increased level of stromal cells with fibroblast and myo-fibroblast phenotype and reduced levels of smooth muscle actin cells were observed in proliferative cancerous tissue of prostate [85]. In-vitro studies have shown the ability of prostate fibroblasts to transform into myo-fibroblast cells [86, 87]. While the label-free nature of SLIM prevents us from knowing the exact molecular or morphological change that leads to the increased diversity we see in the anisotropy measurement, all the changes documented with immunohistochemistry would contribute to increased disorganization in the stroma which we measure as optical anisotropy. One advantage of SLIM is that we can measure the final effect of all the molecular changes which cannot be done in immunohistochemistry due to its inherent reactive nature.

In grade 4 adenocarcinoma, we see that there is a wide distribution range of anisotropy values. This could be due to increased invasiveness seen in some Gleason grade 4 cancers [55]. The importance of stromal changes in cancer outcomes and invasiveness has been demonstrated in the breast and colon in the past [78, 88-91] and a preliminary study done in our lab shows that the stroma adjoining glands is indicative of tumor aggressiveness.

The importance of stromal regulation of prostatic epithelium has been demonstrated in in-vitro studies in the past. Prostate epithelium cultured on reconstituted extra-cellular matrix showed increased levels of prostate specific antigen and prostatic acid phosphatase as opposed to increased cell growth and reduced PSA, PAP levels seen in cells grown on plastic plates [92]. In our study, we saw changes in the single layer of stroma adjoining glandular epithelium. This might be indicative of stroma-epithelial cross-talk previously seen in literature.

Our results are significant since this is the first time, to our knowledge, that differences were seen in stroma in label-free images of prostate cancer cores of various Gleason grades. Further studies need to be done to explore the prognostic significance of the stromal diversity seen in various Gleason grades. Also, with the addition of new parameters, we might be able to quantitatively differentiate between Gleason grade 3 and 4 adenocarcinoma proving to be a valuable tool for pathologists.

5.4 Optical changes in prostate nuclei[11]

5.4.1 Motivation

In clinical practice, the nuclear aspects that are of interest to pathologists are nuclear size and shape, mitotic count, nucleolar count and chromatin changes. In a wide range of cancers, lobulation of nuclei, asymmetric arrangement of heterochromatin aggregates, irregular folds in nuclear membrane, enlarged nucleoli and cell-to-cell variation in number of nucleoli are hallmarks of cancer [93]. While prostate cancer and PIN (prostatic intra-epithelial neoplasia) is characterized by increased nucleolar count and prominently basal nucleoli, nuclear properties are not a part of the Gleason grading system.

We used quantitative phase imaging methods to study changes in nuclei in unstained tissue increasing Gleason grades. We characterized changes in the dry mass, dry mass density and area of the nucleus from quantitative phase images obtained from SLIM. We also studied the spatial organization of the nucleus by studying the spatial scattering of light passing through the nuclei. Our results show that there is a change in nuclear dry mass of cancerous and normal tissue; and spatial scattering spectrum can be used to separate tissue of varying Gleason grades.

5.4.2 Materials and Methods

We obtained tissue microarray (TMA) set from the Cooperative Prostate Cancer Tissue Resource (CPCTR) database. For our analysis, we had 2 patients with benign prostatic hyperplasia (BPH), 1 patient with Gleason score 4 (2+2) adenocarcinoma, 1 patient with Gleason score 6 (3+3) adenocarcinoma, 1 patient with Gleason score 7 (4+3) adenocarcinoma and 1 patient with Gleason score 8 (4+4) adenocarcinoma. They were grouped into three groups for analysis

[11] The text in this section is adapted from:
Sridharan, S., Pham, H., Wickland, D., Tangella, K., Macias, V., Kajdacsy-Balla,A., Popescu, G., FTLS of nucleus during prostate cancer progression (manuscript in preparation)

purposes: “BPH” with 2 patients with benign prostatic hyperplasia, “low-grade tumor” with the patients with Gleason scores 4 and 6 and “high-grade tumors” with the patients with Gleason scores 7 and 8. Each core had 150-800 nuclei that were used in our analysis. We used benign prostatic hyperplasia (BPH) tissue as control due to its high incidence in the demographic affected by prostate cancer. BPH affects 50-60% of men in their 60s and 80-90% of men in their 70s; and the median age for patients with prostate cancer is 67 years [38, 94]. While Gleason score 7 is usually considered intermediate risk, we categorized our patient as high-grade cancer since his Gleason score was 4+3 which is associated with worse prognosis that 3+4 [55].

The unstained tissue microarray slides were imaged using the 40X/0.75NA objective in SLIM. The mosaic feature on Zeiss was used to image each core which was approximately 100 frames. The mosaic feature can be adjusted to set up multiple focus planes, ensuring that all sample areas are in focus. The images were stitched together using an ImageJ plugin built in-house and individual cores were cropped out to the size of 10000x10000 pixels which is approximately 100 frames stitched together (Fig 13.1).

The images were segmented using a Wacom tablet, ImageJ and plug-in built in our lab. Individual nuclei were isolated as regions of interest (ROI) manually using a Wacom tablet. Our in-house plugin crops and pastes the phase images of the isolated nuclei in a zero-phase background image in their original positions (Fig 13.3). This allows us to study the spatial light scattering of the nuclei.

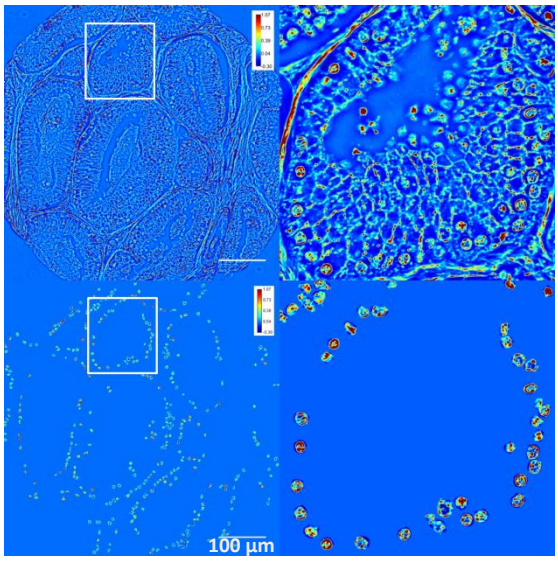

Figure 13[12]: Top Left: 40X SLIM image of prostate TMA core with Gleason score 4 (2+2) adenocarcinoma with the highlighted area zoomed in on Top Right image. Bottom Left: Isolated Nuclei from the image on Top Left, with the highlighted area zoomed in on Bottom Right image.

5.4.3 Results

5.4.3.1 Nuclear Dry Mass Density, Area of Nucleus and Nuclear Dry Mass

In order to study the nuclear changes that occur in prostate cancer we studied the distribution of nuclear area, nuclear density and the dry mass of nucleus. The nuclear area was calculated by manually segmenting the nucleus and using ImageJ to measure the area of each nucleus. We found that the area of the nucleus increases in higher grade nuclei (Gleason score 7 and 8) when compared to that of benign prostatic hyperplasia patients (t-test, p=2.42E-10). However, the nuclear area of low-grade cancer is comparable to that of BPH while significantly lower than high-grade cancer nuclei (t-test, p=1.19E-79). We compared the nuclear density which is related to phase value by the following relation:

[12] Figure reprinted from **Sridharan, S.**, Pham, H., Wickland, D., Tangella, K., Macias, V., Kajdacsy-Balla,A., Popescu, G., FTLS of nucleus during prostate cancer progression (manuscript in preparation)

$$\rho(x.y) = \frac{\lambda}{2\pi\gamma}\Phi(x,y)$$

where φ is the phase value measured by SLIM in radians and γ =0.2ml/g is the refractive increment. We found that the nuclear density is increased in lower grade cancer (Gleason score 4, 6) when compared with BPH nuclei (t-test, p=1.6E-57). In higher grade cancer, the nuclear density is comparable to that of BPH nuclei but significantly different from that of lower grade cancer (t-test, p=1.82E-50).

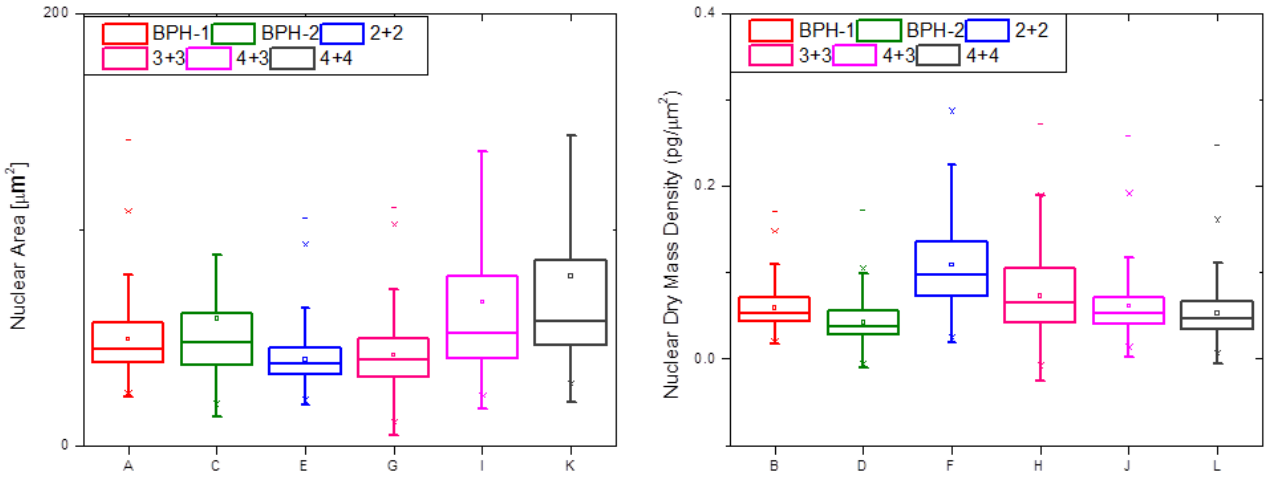

Figure 14[13]: Left: Illustrates the differences in the distribution of nuclear area among prostate cancer cores of various grades Right: Illustrates the differences in the distribution of nuclear dry mass densities among the various progression groups.

Nuclear dry mass in all grades of prostate cancer is higher than that of BPH due to the increased mass density in lower grade cancer and higher nuclear area in high grade cancers (t-test, p=2.13E-25).

[13] Figure reprinted from **Sridharan, S.**, Pham, H., Wickland, D., Tangella, K., Macias, V., Kajdacsy-Balla,A., Popescu, G., FTLS of nucleus during prostate cancer progression (manuscript in preparation)

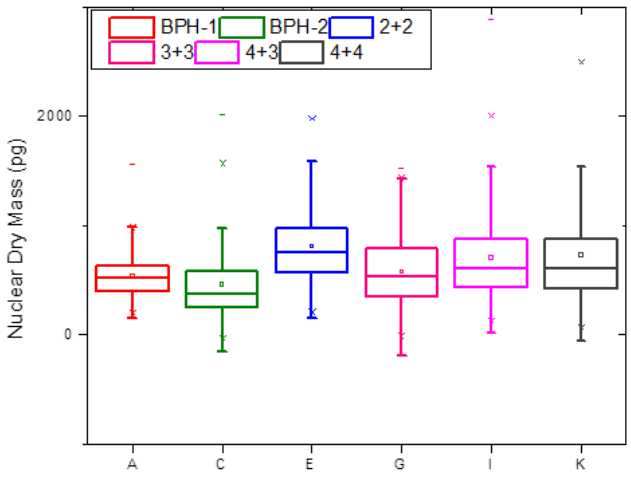

Figure 15[14]: The nuclear dry mass is comparable among all the cancer groups but is significantly greater than the control (BPH) group nuclear dry mass.

5.4.3.2 FTLS Study of Prostate Cancer Progression

We obtained the power spectrum of the phase images of the nuclei since these provide us with spatial scattering information at different length scales. We calculated the point spread function using a 40X SLIM image and normalized the spatial scattering image of the nuclei. We also did additional normalization to account for differences in amount of nuclei in each sample by normalization with a 1-D area obtained from the power spectrum images.

We see multiple peaks in the low frequency (high length scale) region that corresponds to nucleus size and the peak is pushed to lower frequencies when multiple nuclei are in close proximity as seen in the Gleason score 4 adenocarcinoma patient. In the higher frequency region, we obtain information regarding the nucleolar distribution and nuclear envelope continuity. We notice that the peaks are arranged in the high-frequency region corresponding to

[14] Figure reprinted from **Sridharan, S.**, Pham, H., Wickland, D., Tangella, K., Macias, V., Kajdacsy-Balla,A., Popescu, G., FTLS of nucleus during prostate cancer progression (manuscript in preparation)

6 radians/micron and 10 radians/micron in order of increasing severity with the only anomaly being the Gleason score 4 patient.

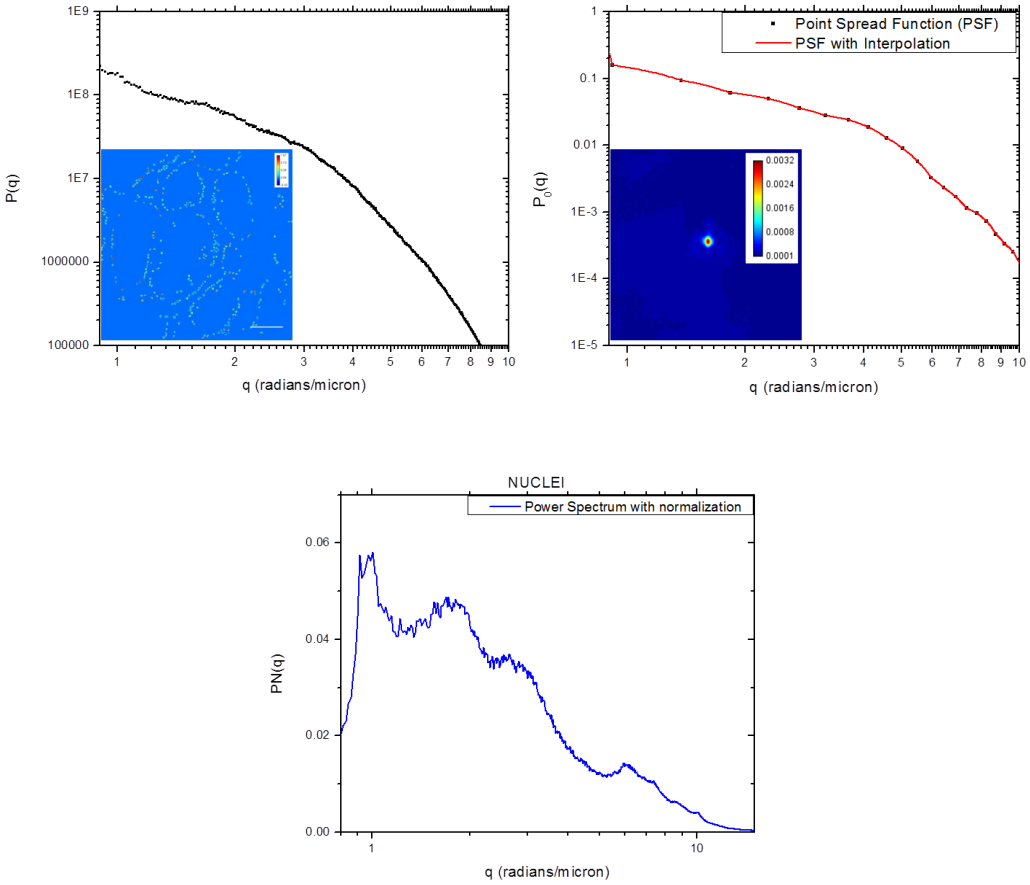

Figure 16[15]: Top left: This shows the angular power spectrum for nuclei from Gleason score 4 (2+2) without any normalization, the inset shows the QPI image of the case. Top right: In inset shows the point-spread function (PSF) and the curves show the measured and interpolated point spread function. Bottom: Shows the normalized version of the power spectrum for the Gleason score 4 QPI image, where it has been normalized for both PSF and 1D area of the nuclei.

[15] Figure reprinted from **Sridharan, S.**, Pham, H., Wickland, D., Tangella, K., Macias, V., Kajdacsy-Balla,A., Popescu, G., FTLS of nucleus during prostate cancer progression (manuscript in preparation)

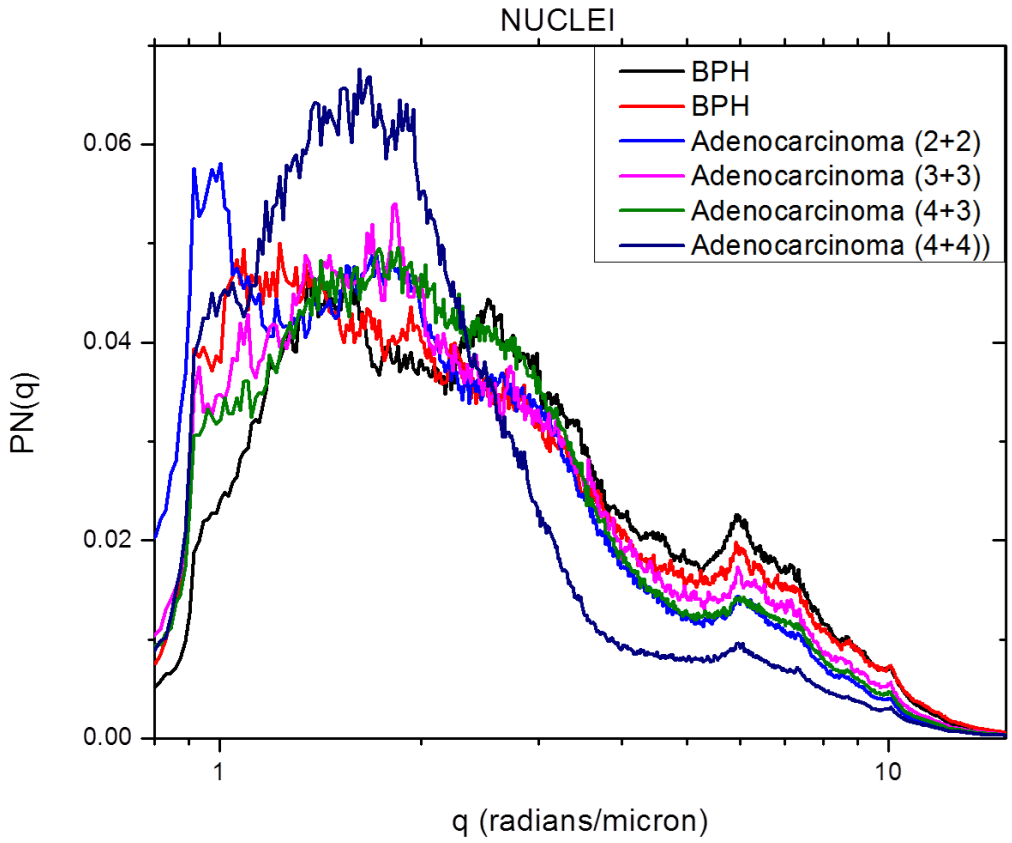

Figure 17[16]: This shows the normalized power spectrum for the nuclei from various progression groups and in high frequency regions they align in order of increasing severity.

5.4.4 Discussion

Our results show that nuclear density is increased in low grade cancers whereas nuclear area is increased in higher grade cancers. Previous studies have documented that nucleolar size is smaller in fast-growing tumors and is bigger in slow-growing prostate lesions [95]. Nucleolar count increase is also indicative of highly proliferative tumors since they are a reflection of ribosome production [96, 97]. Nuclear morphology is primarily determined by nuclear matrix proteins and lamins. A study by Partin et. Al. showed a nuclear matrix protein PC1 was present in cancer nuclei but not in normal or BPH nuclei [98-101]. The nuclear lamina serves as

[16] Figure reprinted from **Sridharan, S.**, Pham, H., Wickland, D., Tangella, K., Macias, V., Kajdacsy-Balla,A., Popescu, G., FTLS of nucleus during prostate cancer progression (manuscript in preparation)

attachment points for heterochromatin on the inner surface and also determines nuclear shape. Nuclear shape changes in papillary thyroid carcinoma with corresponding aggregation changes of heterochromatin has been documented before [93]. A change in nuclear matrix proteins would alter nuclear shape, whereas a change in nuclear lamin proteins would change nuclear density and nuclear shape. It is not surprising that nuclear density would increase due to increase in the number of nucleoli since this is also a result of increased cellular proliferation and therefore DNA multiplication. All of these explain the changes in nuclear density and area.

The low frequency region in the nuclear spectroscopy reflects the nuclear size. As expected from the nuclear analysis, the nuclear size is bigger in higher cancer grades. The multiple peaks in this region, correspond to multiple nuclei adjacent to each other which is caused by increased proliferation seen in cancer. In the higher frequency region (>5rad/micron), the spatial spectroscopy results organize the different grades of prostate disease in order of severity. Since the information we obtain from phase images is related to dry protein distributions we think we measure information related to nuclear envelope discontinuities, nucleolar count and nuclear matrix protein distributions. The spatial spectroscopy also summarizes the results from the nuclear density and area studies. Study of spatial scattering from nuclei could prove to be a valuable pathological tool. However, the data we studied here is limited and further studies need to be done to explore the clinical utility of this tool.

6. Summary & Future Work

Prostate cancer has a very high incidence rate and the diagnostic process is expensive due to the use of expensive immunohistochemical markers. Qualitative imaging methods such as GFM make the diagnosis of prostate cancer without the additional cost and delay associated with current clinical pathology practice. Quantitative phase imaging methods such as SLIM combined with FTLS can detect very sensitive changes in tissue architecture without the use of stains. We were able to show changes in both prostate nuclei and stroma in the intermediate risk categories where Gleason grading does not provide good prognostic measure.

These methods show potential for a multitude of future applications:

1. **Gleason Grading:** Studies have shown that urologic pathologists show a consensus of 70% on Gleason grades whereas among general pathologists the consensus drops below 50% for Gleason scores 5-7 [60, 61]. Since the Gleason grades determine the course of treatment, a more objective method is necessary to perform grading and remove inter-observer variability. QPI techniques can be used for this purpose.
2. **Prediction of prostate cancer recurrence:** The current gold-standard to predict recurrence of prostate cancer is the CAPRA-S nomogram developed in University of California San Fransisco. However, CAPRA-S discrimination is low in the D'Amico intermediate risk category. Using QPI, we were able to detect changes in stroma among patients in this category, but we had no recurrence information associated with those patients. We believe that QPI might have the sensitivity to improve the accuracy of recurrence prediction in this intermediate risk group.
3. **Field Effect Detection:** There are instances where prostate cancer is not detected in a biopsy but is diagnosed in a repeat biopsy at an advanced stage. This could be due to a

sampling error at the biopsy stage. A sensitive tool that can detect pre-malignant changes and field effect associated with prostate cancer can solve this problem. QPI shows promise in this area.

References

1. Fischer, A.H., et al., *Hematoxylin and eosin staining of tissue and cell sections.* CSH Protoc, 2008. **2008**: p. pdb prot4986.
2. Zernike, F., *How I discovered phase contrast.* Science, 1955. **121**(3141): p. 345-9.
3. Wang, Z., et al., *Topography and refractometry of nanostructures using spatial light interference microscopy.* Opt Lett. **35**(2): p. 208-10.
4. Bohren, C.F. and D.R. Huffman, *Absorption and scattering of light by small particles*1983, New York: Wiley. xiv, 530 p.
5. Hulst, H.C.v.d., *Light scattering by small particles*1981, New York: Dover Publications. 470 p.
6. Ishimaru, A., *Electromagnetic wave propagation, radiation, and scattering*1991, Englewood Cliffs, N.J.: Prentice Hall. xviii, 637 p.
7. Berne, B.J. and R. Pecora, *Dynamic light scattering with applications to chemistry, biology and Physics*1976, New York: Wiley.
8. Zhu, R., et al., *Correlation-induced spectral changes in tissues.* Opt Lett. **36**(21): p. 4209-11.
9. *Milestones in light microscopy.* Nat Cell Biol, 2009. **11**(10): p. 1165-1165.
10. Alberts, B., *Essential cell biology : an introduction to the molecular biology of the cell*. 2 ed2004, New York: Garland Pub. 1 v. (various pagings).
11. Dunn, A. and R. Richards-Kortum, *Three-dimensional computation of light scattering from cells.* Ieee Journal of Selected Topics in Quantum Electronics, 1996. **2**(4): p. 898-905.
12. Mourant, J.R., et al., *Mechanisms of light scattering from biological cells relevant to noninvasive optical-tissue diagnostics.* Applied Optics, 1998. **37**(16): p. 3586-3593.
13. Hale, G.M. and M.R. Querry, *Optical-Constants of Water in 200-Nm to 200-Mum Wavelength Region.* Applied Optics, 1973. **12**(3): p. 555-563.
14. Takatani, S. and M.D. Graham, *Theoretical-Analysis of Diffuse Reflectance from a 2-Layer Tissue Model.* Ieee Transactions on Biomedical Engineering, 1979. **26**(12): p. 656-664.
15. Wang, Z., H. Ding, and G. Popescu, *Scattering-phase theorem.* Optics Letters, 2011. **36**: p. 1215.
16. Ding, H., et al., *Measuring the scattering parameters of tissues from quantitative phase imaging of thin slices.* Optics Letters, 2011. **36**: p. 2281.
17. Wolf, E., *Invariance of the Spectrum of Light on Propagation.* Physical Review Letters, 1986. **56**(13): p. 1370-1372.
18. Bocko, M.F., D.H. Douglass, and R.S. Knox, *Observation of Frequency-Shifts of Spectral-Lines Due to Source Correlations.* Physical Review Letters, 1987. **58**(25): p. 2649-2651.
19. Wolf, E., *Non-Cosmological Redshifts of Spectral-Lines.* Nature, 1987. **326**(6111): p. 363-365.
20. Wolf, E., J.T. Foley, and F. Gori, *Frequency-Shifts of Spectral-Lines Produced by Scattering from Spatially Random-Media.* Journal of the Optical Society of America a-Optics Image Science and Vision, 1989. **6**(8): p. 1142-1149.
21. Dogariu, A. and E. Wolf, *Spectral changes produced by static scattering on a system of particles.* Opt. Lett., 1998. **23**(17): p. 1340-1342.

22. Frick, J. and W. Aulitzky, *Physiology of the prostate.* Infection, 1991. **19 Suppl 3**: p. S115-8.
23. McNeal, J.E., *Anatomy of the prostate: An historical survey of divergent views.* The Prostate, 1980. **1**(1): p. 3-13.
24. McNeal, J.E., *Regional morphology and pathology of the prostate.* American journal of clinical pathology, 1968. **49**(3): p. 347-57.
25. McNeal, J.E., *Origin and development of carcinoma in the prostate.* Cancer, 1969. **23**(1): p. 24-34.
26. McNeal, J.E., *Origin and evolution of benign prostatic enlargement.* Investigative urology, 1978. **15**(4): p. 340-5.
27. Hadley, H.L., *Physiology of the prostate.* Medical arts and sciences, 1952. **6**(1): p. 22-3.
28. Farnsworth, W.E., *Prostate stroma: physiology.* The Prostate, 1999. **38**(1): p. 60-72.
29. Roehrborn C, M.J., *Etiology, pathophysiology, epidemiology and natural history of benign prostatic hyperplasia*, in *Campbell's Urology*, R.A. Walsh P, Vaughan E, Wein A Editor 2002, Saunders: Philadelphia. p. 1297-1336.
30. Roehrborn, C.G., *Pathology of benign prostatic hyperplasia.* Int J Impot Res, 2008. **20 Suppl 3**: p. S11-8.
31. Bostwick, D.G., et al., *High-grade prostatic intraepithelial neoplasia.* Rev Urol, 2004. **6**(4): p. 171-9.
32. Bostwick, D.G. and M.K. Brawer, *Prostatic intra-epithelial neoplasia and early invasion in prostate cancer.* Cancer, 1987. **59**(4): p. 788-94.
33. Epstein, J.I. and G.J. Netto, *Biopsy Interpretation of the Prostate*2007: Lippincott Williams & Wilkins.
34. Epstein, J.I. and M. Herawi, *Prostate needle biopsies containing prostatic intraepithelial neoplasia or atypical foci suspicious for carcinoma: implications for patient care.* J Urol, 2006. **175**(3 Pt 1): p. 820-34.
35. Jemal, A., et al., *Cancer statistics, 2010.* CA Cancer J Clin. **60**(5): p. 277-300.
36. Howlader N, N.A., Krapcho M, Neyman N, Aminou R, Altekruse SF, Kosary CL, Ruhl J, Tatalovich Z, Cho H, Mariotto A, Eisner MP, Lewis DR, Chen HS, Feuer EJ, Cronin KA. *SEER Cancer Statistics Review, 1975-2009*. 2011 2012 [cited 2012 November, 10].
37. Welch, H.G. and P.C. Albertsen, *Prostate cancer diagnosis and treatment after the introduction of prostate-specific antigen screening: 1986-2005.* Journal of the National Cancer Institute, 2009. **101**(19): p. 1325-9.
38. *Screening for prostate cancer: U.S. Preventive Services Task Force recommendation statement.* Annals of internal medicine, 2008. **149**(3): p. 185-91.
39. Moyer, V.A., *Screening for prostate cancer: U.S. Preventive Services Task Force recommendation statement.* Annals of internal medicine, 2012. **157**(2): p. 120-34.
40. Sakr, W.A., et al., *The frequency of carcinoma and intraepithelial neoplasia of the prostate in young male patients.* The Journal of urology, 1993. **150**(2 Pt 1): p. 379-85.
41. Gronberg, H., *Prostate cancer epidemiology.* Lancet, 2003. **361**(9360): p. 859-64.
42. Force, U.S.P.S.T. *Screening for prostate cancer: final recommendation statement*. [cited 2012 November, 10].
43. Gleason, D.F., *Classification of prostatic carcinomas.* Cancer Chemother Rep, 1966. **50**(3): p. 125-8.
44. Humphrey, P.A., *Gleason grading and prognostic factors in carcinoma of the prostate.* Mod Pathol, 2004. **17**(3): p. 292-306.

45. Epstein, J.I., et al., *Prediction of progression following radical prostatectomy. A multivariate analysis of 721 men with long-term follow-up.* Am J Surg Pathol, 1996. **20**(3): p. 286-92.
46. Partin, A.W., et al., *Combination of prostate-specific antigen, clinical stage, and Gleason score to predict pathological stage of localized prostate cancer. A multi-institutional update.* JAMA, 1997. **277**(18): p. 1445-51.
47. Egevad, L., et al., *Prognostic value of the Gleason score in prostate cancer.* BJU Int, 2002. **89**(6): p. 538-42.
48. Gleason, D.F. and G.T. Mellinger, *Prediction of prognosis for prostatic adenocarcinoma by combined histological grading and clinical staging. 1974.* J Urol, 2002. **167**(2 Pt 2): p. 953-8; discussion 959.
49. Gleason, D.F. and G.T. Mellinger, *Prediction of prognosis for prostatic adenocarcinoma by combined histological grading and clinical staging.* J Urol, 1974. **111**(1): p. 58-64.
50. Gleason, D.F., *Undergrading of prostate cancer biopsies: a paradox inherent in all biologic bivariate distributions.* Urology, 1996. **47**(3): p. 289-91.
51. Pan, C.C., et al., *The prognostic significance of tertiary Gleason patterns of higher grade in radical prostatectomy specimens: a proposal to modify the Gleason grading system.* The American journal of surgical pathology, 2000. **24**(4): p. 563-9.
52. Epstein, J.I., et al., *The 2005 International Society of Urological Pathology (ISUP) Consensus Conference on Gleason Grading of Prostatic Carcinoma.* The American journal of surgical pathology, 2005. **29**(9): p. 1228-42.
53. Amin, M.B., D.S. Schultz, and R.J. Zarbo, *Analysis of cribriform morphology in prostatic neoplasia using antibody to high-molecular-weight cytokeratins.* Archives of pathology & laboratory medicine, 1994. **118**(3): p. 260-4.
54. Ghani, K.R., et al., *Trends in reporting Gleason score 1991 to 2001: changes in the pathologist's practice.* European urology, 2005. **47**(2): p. 196-201.
55. Makarov, D.V., et al., *Gleason score 7 prostate cancer on needle biopsy: is the prognostic difference in Gleason scores 4 + 3 and 3 + 4 independent of the number of involved cores?* The Journal of urology, 2002. **167**(6): p. 2440-2.
56. Grober, E.D., et al., *Correlation of the primary Gleason pattern on prostate needle biopsy with clinico-pathological factors in Gleason 7 tumors.* The Canadian journal of urology, 2004. **11**(1): p. 2157-62.
57. Merrick, G.S., et al., *Biochemical outcome for hormone-naive intermediate-risk prostate cancer managed with permanent interstitial brachytherapy and supplemental external beam radiation.* Brachytherapy, 2002. **1**(2): p. 95-101.
58. Merrick, G.S., et al., *Biochemical outcome for hormone-naive patients with Gleason score 3+4 versus 4+3 prostate cancer undergoing permanent prostate brachytherapy.* Urology, 2002. **60**(1): p. 98-103.
59. Gonzalgo, M.L., et al., *Relationship between primary Gleason pattern on needle biopsy and clinicopathologic outcomes among men with Gleason score 7 adenocarcinoma of the prostate.* Urology, 2006. **67**(1): p. 115-9.
60. Allsbrook, W.C., Jr., et al., *Interobserver reproducibility of Gleason grading of prostatic carcinoma: urologic pathologists.* Human pathology, 2001. **32**(1): p. 74-80.
61. Allsbrook, W.C., Jr., et al., *Interobserver reproducibility of Gleason grading of prostatic carcinoma: general pathologist.* Human pathology, 2001. **32**(1): p. 81-8.
62. Zernike, F., *How I discovered phase contrast.* Science, 1955. **121**: p. 345.

63. Gabor, D., *A new microscopic principle.* Nature, 1948. **161**: p. 777.
64. Wang, Z., et al., *Spatial light interference microscopy (SLIM).* Optics Express, 2011. **19**(2): p. 1016.
65. Mir, M., et al., *Measuring Cell Cycle-Dependent Mass Growth* Proc. Nat. Acad. Sci., 2011. **108**(32): p. 13124.
66. Popescu, G., et al., *Label-free intracellular transport measured by spatial light interference microscopy.* Journal of Biomedical Optics, 2011. **16**(2).
67. Wang, R., et al., *One-dimensional deterministic transport in neurons measured by dispersion-relation phase spectroscopy.* J. Phys.: Cond. Matter, 2011. **23**: p. 374107.
68. Babacan, S.D., et al., *Cell imaging beyond the diffraction limit using sparse deconvolution spatial light interference microscopy.* Biomed Opt Express. **2**(7): p. 1815-27.
69. Ding, H.F., et al., *Fourier Transform Light Scattering of Biological Structure and Dynamics.* Ieee Journal of Selected Topics in Quantum Electronics, 2010. **16**(4): p. 909-918.
70. Ding, H.F., et al., *Fourier Transform Light Scattering (FTLS) of Cells and Tissues.* Journal of Computational and Theoretical Nanoscience, 2010. **7**(12): p. 2501-2511.
71. Tuxhorn, J.A., et al., *Reactive stroma in human prostate cancer: induction of myofibroblast phenotype and extracellular matrix remodeling.* Clinical cancer research : an official journal of the American Association for Cancer Research, 2002. **8**(9): p. 2912-23.
72. *Guidebook to the extracellular matrix and adhesion proteins Edited by T Kreis and R Vale. pp 176. Oxford University Press. 1993. £40 or £18.50 (pbk) ISBN 0-19-859934-X or -859933-1s.* Biochemical Education, 1993. **21**(4): p. 209-210.
73. Taipale, J. and J. KeskiOja, *Growth factors in the extracellular matrix.* Faseb Journal, 1997. **11**(1): p. 51-59.
74. Tuxhorn, J.A., G.E. Ayala, and D.R. Rowley, *Reactive stroma in prostate cancer progression.* The Journal of urology, 2001. **166**(6): p. 2472-83.
75. Noel, A. and J.M. Foidart, *The role of stroma in breast carcinoma growth in vivo.* Journal of mammary gland biology and neoplasia, 1998. **3**(2): p. 215-25.
76. Gregoire, M. and B. Lieubeau, *The role of fibroblasts in tumor behavior.* Cancer metastasis reviews, 1995. **14**(4): p. 339-50.
77. Ayala, G., et al., *Reactive stroma as a predictor of biochemical-free recurrence in prostate cancer.* Clinical cancer research : an official journal of the American Association for Cancer Research, 2003. **9**(13): p. 4792-801.
78. Ronnov-Jessen, L., O.W. Petersen, and M.J. Bissell, *Cellular changes involved in conversion of normal to malignant breast: importance of the stromal reaction.* Physiol Rev, 1996. **76**(1): p. 69-125.
79. Rowley, D.R., *What might a stromal response mean to prostate cancer progression?* Cancer metastasis reviews, 1998. **17**(4): p. 411-9.
80. Schmitt-Graff, A., A. Desmouliere, and G. Gabbiani, *Heterogeneity of myofibroblast phenotypic features: an example of fibroblastic cell plasticity.* Virchows Archiv : an international journal of pathology, 1994. **425**(1): p. 3-24.
81. Seemayer, T.A., et al., *Myofibroblasts in the stroma of invasive and metastatic carcinoma: a possible host response to neoplasia.* The American journal of surgical pathology, 1979. **3**(6): p. 525-33.

82. Lipponen, P., et al., *High stromal hyaluronan level is associated with poor differentiation and metastasis in prostate cancer.* Eur J Cancer, 2001. **37**(7): p. 849-56.
83. Hagglof, C., et al., *Stromal PDGFRbeta expression in prostate tumors and non-malignant prostate tissue predicts prostate cancer survival.* PLoS One. **5**(5).
84. McAlhany, S.J., et al., *Decreased stromal expression and increased epithelial expression of WFDC1/ps20 in prostate cancer is associated with reduced recurrence-free survival.* Prostate, 2004. **61**(2): p. 182-91.
85. Hayward, S.W., G.R. Cunha, and R. Dahiya, *Normal development and carcinogenesis of the prostate. A unifying hypothesis.* Annals of the New York Academy of Sciences, 1996. **784**: p. 50-62.
86. Peehl, D.M. and R.G. Sellers, *Induction of smooth muscle cell phenotype in cultured human prostatic stromal cells.* Experimental cell research, 1997. **232**(2): p. 208-15.
87. Gerdes, M.J., et al., *Regulation of rat prostate stromal cell myodifferentiation by androgen and TGF-beta1.* The Prostate, 2004. **58**(3): p. 299-307.
88. Ronnov-Jessen, L. and O.W. Petersen, *Induction of alpha-smooth muscle actin by transforming growth factor-beta 1 in quiescent human breast gland fibroblasts. Implications for myofibroblast generation in breast neoplasia.* Lab Invest, 1993. **68**(6): p. 696-707.
89. Brown, L.F., et al., *Vascular stroma formation in carcinoma in situ, invasive carcinoma, and metastatic carcinoma of the breast.* Clin Cancer Res, 1999. **5**(5): p. 1041-56.
90. Lagace, R., et al., *Myofibroblastic stromal reaction in carcinoma of the breast: variations of collagenous matrix and structural glycoproteins.* Virchows Arch A Pathol Anat Histopathol, 1985. **408**(1): p. 49-59.
91. Martin, M., P. Pujuguet, and F. Martin, *Role of stromal myofibroblasts infiltrating colon cancer in tumor invasion.* Pathol Res Pract, 1996. **192**(7): p. 712-7.
92. Fong, C.J., et al., *Reconstituted Basement-Membrane Promotes Morphological and Functional-Differentiation of Primary Human Prostatic Epithelial-Cells.* Prostate, 1991. **19**(3): p. 221-235.
93. Zink, D., A.H. Fischer, and J.A. Nickerson, *Nuclear structure in cancer cells.* Nature reviews. Cancer, 2004. **4**(9): p. 677-87.
94. Roehrborn, C.G., *Benign prostatic hyperplasia: an overview.* Reviews in urology, 2005. **7 Suppl 9**: p. S3-S14.
95. Fischer, A.H., S. Bardarov, Jr., and Z. Jiang, *Molecular aspects of diagnostic nucleolar and nuclear envelope changes in prostate cancer.* J Cell Biochem, 2004. **91**(1): p. 170-84.
96. Fischer, A.H., S. Bardarov, Jr., and Z. Jiang, *Molecular aspects of diagnostic nucleolar and nuclear envelope changes in prostate cancer.* Journal of cellular biochemistry, 2004. **91**(1): p. 170-84.
97. Derenzini, M., et al., *Nucleolar size indicates the rapidity of cell proliferation in cancer tissues.* The Journal of pathology, 2000. **191**(2): p. 181-6.
98. Partin, A.W., et al., *Preliminary immunohistochemical characterization of a monoclonal antibody (PRO:4-216) prepared from human prostate cancer nuclear matrix proteins.* Urology, 1997. **50**(5): p. 800-8.
99. Partin, A.W., et al., *Nuclear matrix protein patterns in human benign prostatic hyperplasia and prostate cancer.* Cancer Res, 1993. **53**(4): p. 744-6.

100. Leman, E.S. and R.H. Getzenberg, *Nuclear matrix proteins as biomarkers in prostate cancer*. J Cell Biochem, 2002. **86**(2): p. 213-23.
101. Subong, E.N., et al., *Monoclonal antibody to prostate cancer nuclear matrix protein (PRO:4-216) recognizes nucleophosmin/B23.* Prostate, 1999. **39**(4): p. 298-304.